Continuously Adjustable Cylindrical Vector and Vortex Beams by Programming Vortex Half-Wave Plates and Detection Based on Coaxial or Small-Angle Interference

Junli Qi,[1,2,3,4,*] Wenjun Yi,[1] Meicheng Fu,[1] Ju Liu,[1,5] Mengjun Zhu,[1] Shuyue Zhu,[1] Xin Chen,[1] Hongyu Zhang,[1] Hui Zhang,[4] Bo Shi,[4] Wenjing Pu,[4] Haifei Deng,[4] Weihua Wang,[2,3,4,6,†] and Xiujian Li[1,‡]

[1] *College of Science, National University of Defense Technology, Changsha 410073, China*
[2] *Institute of Plasma Physics, Hefei Institutes of Physical Sciences, Chinese Academy of Sciences, Hefei 230031, China*
[3] *Science Island Branch of Graduate School, University of Science and Technology of China, Hefei 230031, China*
[4] *Basic Department, Army Academy of Artillery and Air Defense, Hefei 230031, China*
[5] *Hunan Institute of Traffic Engineering, Hengyang 421099, China*
[6] *Institute of Physical Science and Information Technology, Anhui University, Hefei 230031, China*

(Received 8 July 2022; revised 8 August 2022; accepted 6 September 2022; published 30 September 2022)

A convenient and versatile scheme to generate continuously adjustable cylindrical vector (CV) and vortex beams by multiplexing and cascading passive vortex half-wave plates (VHPs) is proposed. (−24)–24 order CV or vortex beams are generated only based on VHPs with $m = 1$, 3, and 8. The coaxial and small-angle interference are introduced to detect orders. For coaxial interference of l_1-order and l_2-order vortex beams, the intensity distribution is spirally fan shaped. The partition number is $N = |l_2 - l_1|$, and the spiral direction can distinguish the sign of topological charge with higher value. Fork-shaped fringes appear in the center for small-angle interference between vortex beams with incident angle β_1 and β_2. The forking number between two fringes meets $N = |l_2 - l_1|$, and the forks face upward when $(l_2 - l_1)(\beta_2 - \beta_1) < 0$, and face downward when $(l_2 - l_1)(\beta_2 - \beta_1) > 0$. Particularly, when one of the beams is a Gaussian beam, such as $l_1 = 0$, the value and sign of the topological charge l_2 can be directly detected. And for the interference between CV and Gaussian plane beams, the partition number N is positively correlated with the polarization order P, with $N = |P|$ or $N = 2|P|$ for coaxial or small-angle interference, respectively, and corresponding sign can be identified by the polarization azimuth distributions measured by Stokes parameters. It is experimentally demonstrated that the proposed scheme can effectively generate continuously adjustable CV and vortex beams by programming limited VHPs, greatly expanding order numbers with low cost, low energy consumption, and high utilization, and the coaxial and small-angle interference method can conveniently detect the corresponding orders without borrowing redundant devices.

DOI: 10.1103/PhysRevApplied.18.034086

I. INTRODUCTION

The cylindrical vector (CV) and vortex beams have attracted widespread attention due to a donut intensity distributions and cylindrically symmetric polarization or helical phase wave-front properties [1–4]. Due to the orbital angular momentum carried by the optical field around them, they have found applications in fields such as particle trapping and manipulating [5–7], tight focusing and beam shaping [8,9], laser materials processing [10,11], superresolution techniques [12,13], optical communication [14–18], quantum information process [19–22], reverse flow [23,24] and fiber and integrated optics [25–30], and so on.

Multiple methods and schemes are proposed to generate CV and vortex beams, including intracavity and extracavity techniques. The intracavity methods have the advantages of high quality and energy-conversion efficiency but lack of flexibility due to limited space. The extracavity methods are relatively more flexible and popular with conversion devices such as spiral phase plates [31–35], anisotropic crystals [36–39], diffractive optical elements and digital micromirror device (DMD) [40–43], metasurfaces and q-plates [44–50], Sagnac and Mach-Zehnder interferometers [51–54], photon sieves [55,56] and the most used spatial light modulator (SLM) [57–60].

*qijunli_r@163.com
†whwang@ipp.ac.cn
‡xjli@nudt.edu.cn

But there are more or less problems of stability, complexity, efficiency, cost performance, and so on. For example, the most used SLM or DMD methods have low conversion efficiency due to the diffraction effect and are not cost effective. In addition, they are active energy-consuming devices and require additional power supply.

The detection techniques for vortex beam can be classified mainly into two categories: interference and diffraction. Interference techniques include mainly the Mach-Zehnder interferometer (MZI) [61–63], Sagnac interferometer [64], Fizeau interferometer [65], multipoint interferometer [66], double-slit interferometer [67–69], Talbot interferometer [70,71], and self-reference interferometer [72,73], etc. Diffraction techniques usually use devices such as a triangular aperture [74,75], annular aperture [76,77], diamond-shaped aperture [78], single-slit [79], multi-pinhole plate [80], gratings [81,82] and metasurfaces [83,84], etc. Besides, there are other detection techniques such as geometric coordinate transformation [85,86] and deep learning [87–89], and so on. Among them, the most basic and commonly used device is the MZI, where one vortex beam interferes with another vortex beam or Gaussian plane beam. However, the structure of MZI is still a little complex, requiring two nonpolarized beam splitters (NPBSs), and half the optical energy is wasted with low utilization. And it still needs other unusual devices such as right-angle prism and Dove prism [62,63]. In addition, the in-line interference of conjugate vortex beams cannot distinguish the sign of topological charge [62], and the incident angle direction (positive or negative) about the z axis or the relative incident angle (left or right) about each other is not considered in the off-axis interference between vortex beams, which will affect the forking fringe orientation [63].

Recently, a double-pass configuration has been reported to produce vortex beams [90], which is somewhat similar to our multiplexing technology. However, we finish our work completely independently. Besides, the work of the CV beam is added in our paper, and principles and details are presented to make it clearer and more convincing. Of note, our proposed system avoids multiple use of combination of BS, quarter-wave plate and mirror, which is too redundant, uneconomical, and has large energy loss.

In this paper, continuously adjustable (-24) to 24 order CV and vortex beams are generated by multiplexing the vortex half-wave plates (VHPs) with order $m = 1$, 3, and 8 combined with cascading skill. The VHP is a passive device with a consistent delay π but the direction of the fast axis changing continuously around the center, which has high transmittance and no diffraction effect just like a half-wave plate with high energy conversion. The polarization azimuth (PA) distributions of generated CV beams are investigated by measured Stokes parameters. Besides, the coaxial interference and small-angle interference with Gaussian plane beam are introduced to detect the order of vortex and CV beams. There is only a NPBS in the proposed scheme, which simplifies the system complexity and improves the energy utilization. For the coaxial interference of vortex beams, the interference intensity distribution is spirally fan shaped, and the number N of fan-shape regions equals the absolute value of topological charge l, i.e., $N = |l|$, and positive or negative l has counterclockwise or clockwise direction from the outer tail to center head of fan-shape regions in the central part. The initial phase σ_0 can be adjusted by rotating the quarter-wave plate1 (QP1), which can be discovered by the fan-shape orientation. For the small-angle interference of vortex beams, fringes in the central region bifurcate, and the forking number N between two fringes conforms to $N = |l|$, and the fork faces upward or downward for positive or negative l, respectively, in the experimental condition that the incident angle $\alpha > 0$ of Gaussian beam and $\beta = 0$ of vortex beam. And the forking fringes rotate anticlockwise or clockwise from the outer to center at the bifurcation near the center for positive or negative topological charge l. The initial phase σ_0 adjusted by QP1 can affect the relative forking distribution. And for the interference of CV beams, the partition number N of interference intensity is positively correlated with the polarization order P, with $N = |P|$ for coaxial interference and $N = 2|P|$ for small-angle interference, and the corresponding sign can be identified by the polarization azimuth distributions measured by Stokes parameters. The initial polarization direction ψ_0 adjusted by QP1 will affect the relative interference intensity distribution. It is experimentally demonstrated that the proposed scheme can effectively generate continuously adjustable CV and vortex beam with limited passive VHPs, which can greatly expand the order numbers with low cost, low energy consumption, and high utilization, and the coaxial and small-angle interference method can conveniently detect the corresponding order without borrowing redundant devices.

II. PRINCIPLES

A. Vortex half-wave plate

The VHP is a passive device with a constant retardance π, but its fast axis rotates continuously around the center. The distribution of the fast axis can be described as $\theta = m\varphi/2 + \varphi_0$, in which, φ is the azimuth angle; θ is the VHP fast-axis direction at a certain azimuth angle; m is the integer order number; and φ_0 is the initial fast-axis direction when $\varphi = 0$. The VHP with m and φ_0 can be expresses as VHP(m, φ_0) or VHP(θ) for short. Particularly when $m = 0$, the VHP becomes an ordinary half-wave plate (HP) with the fast axis orientated at φ_0, also called $\boldsymbol{\varphi}_0$ HP, i.e., VHP(0, φ_0) or HP(φ_0). The VHP Jones matrix $J_{\mathrm{VHP}}(\theta)$ with fast axis orientated at the direction θ can be

expressed as

$$J_{\mathrm{VHP}}(\theta) = J_{m,\varphi_0} = \begin{bmatrix} \cos 2\theta & \sin 2\theta \\ \sin 2\theta & -\cos 2\theta \end{bmatrix} = \begin{bmatrix} \cos(m\varphi + 2\varphi_0) & \sin(m\varphi + 2\varphi_0) \\ \sin(m\varphi + 2\varphi_0) & -\cos(m\varphi + 2\varphi_0) \end{bmatrix}, \quad (1)$$

where θ varies with the azimuth angle φ, so the VHP Jones matrix is spatially variable.

B. Continuously adjustable cylindrical vector beams

The Jones vector of a mirror (M) and the **0** HP can be expressed as

$$J_M = \begin{bmatrix} -1 & 0 \\ 0 & 1 \end{bmatrix}, \; J_{\mathrm{HP}}(0) = \begin{bmatrix} 1 & 0 \\ 0 & -1 \end{bmatrix} = e^{i\pi} \times J_M. \quad (2)$$

Since the whole fixed phase difference will not affect the polarization state, it can be considered that $J_M = J_{\mathrm{HP}}(0)$.

When a beam passes through a VHP or quarter-wave plate (QP) from the front, its Jones matrix can be expressed as $J_{\mathrm{VHP}}(\theta)$ or $J_{\mathrm{QP}}(\theta)$, in which θ is the fast-axis direction. And when the beam passes through the same device from the back, its fast-axis direction changes to π–θ from θ, thus, the corresponding Jones matrix becomes $J_{\mathrm{VHP}}(\pi$–$\theta)$ or $J_{\mathrm{QP}}(\pi$–$\theta)$. So, the Jones matrix of VHP and QP in the opposite direction are expressed as the following:

$$\begin{aligned} &J_{\mathrm{VHP}}(\pi - \theta) \\ &\quad = \begin{bmatrix} \cos 2(\pi - \theta) & \sin 2(\pi - \theta) \\ \sin 2(\pi - \theta) & -\cos 2(\pi - \theta) \end{bmatrix} = J_{\mathrm{VHP}}(-\theta) \\ &J_{\mathrm{QP}}(\pi - \theta) \\ &\quad = \frac{\sqrt{2}}{2} \begin{bmatrix} 1 - i\cos 2(\pi - \theta) & -i\sin 2(\pi - \theta) \\ -i\sin 2(\pi - \theta) & 1 + i\cos 2(\pi - \theta) \end{bmatrix} \\ &\quad = J_{\mathrm{QP}}(-\theta). \end{aligned} \quad (3)$$

For better distinction, Q is used to represent the fast-axis direction of a QP. So, when a beam passes through a QP and is vertically reflected by a M, then passes through the same QP from the back again, the corresponding Jones matrix can be expressed as

$$\begin{aligned} &J_{\mathrm{QP}}(-Q) \times J_M \times J_{\mathrm{QP}}(Q) \\ &\quad = \frac{1}{2} \begin{bmatrix} 1 - i\cos 2(-Q) & -i\sin 2(-Q) \\ -i\sin 2(-Q) & 1 + i\cos 2(-Q) \end{bmatrix} \\ &\qquad \times \begin{bmatrix} -1 & 0 \\ 0 & 1 \end{bmatrix} \times \begin{bmatrix} 1 - i\cos 2Q & -i\sin 2Q \\ -i\sin 2Q & 1 + i\cos 2Q \end{bmatrix} \\ &\quad = \frac{1}{2} \begin{bmatrix} 2i\cos 2Q & 2i\sin 2Q \\ -2i\sin 2Q & 2i\cos 2Q \end{bmatrix} \\ &\quad = e^{i\pi/2} \times \begin{bmatrix} \cos 2Q & \sin 2Q \\ -\sin 2Q & \cos 2Q \end{bmatrix} = e^{i\pi/2} \times R'(2Q). \end{aligned} \quad (4)$$

Ignoring the whole $\pi/2$ phase, the combined Jones matrix R' is a counter-rotation matrix. When a linearly polarized (LP) beam with the polarization direction orientated at Φ according to the horizontal direction (x axis), expresses as the Φ LP beam for short, passes through the combined device above, the counter-rotation beam can be obtained with the Jones vector expressed as follows:

$$\begin{aligned} E_{\Phi-2Q} &= R'(2Q) \times E_\Phi = \begin{bmatrix} \cos 2Q & \sin 2Q \\ -\sin 2Q & \cos 2Q \end{bmatrix} \\ &\quad \times \begin{bmatrix} \cos\Phi \\ \sin\Phi \end{bmatrix} \\ &= \begin{bmatrix} \cos 2Q\cos\Phi + \sin 2Q\sin\Phi \\ -\sin 2Q\cos\Phi + \cos 2Q\sin\Phi \end{bmatrix} \\ &= \begin{bmatrix} \cos(\Phi - 2Q) \\ \sin(\Phi - 2Q) \end{bmatrix}. \end{aligned} \quad (5)$$

That is to say, the original polarization direction Φ is rotated by $2Q$ clockwise. The counter rotation means the opposite direction of azimuth angle φ, i.e., clockwise direction.

While when a beam passes through a VHP(θ_1) and a QP(Q) successively and is vertically reflected by a M, then passes through the same QP and VHP from the back again, the corresponding Jones matrix can be expressed as

$$\begin{aligned} &J_{\mathrm{VHP}}(-\theta_1) \times J_{\mathrm{QP}}(-Q) \times J_M \times J_{\mathrm{QP}}(Q) \times J_{\mathrm{VHP}}(\theta_1) \\ &\quad = J_{\mathrm{VHP}}(-\theta_1) \times R'(2Q) \times J_{\mathrm{VHP}}(\theta_1) \\ &\quad = \begin{bmatrix} \cos 2\theta_1 & -\sin 2\theta_1 \\ -\sin 2\theta_1 & -\cos 2\theta_1 \end{bmatrix} \times \begin{bmatrix} \cos 2Q & \sin 2Q \\ -\sin 2Q & \cos 2Q \end{bmatrix} \\ &\qquad \times \begin{bmatrix} \cos 2\theta_1 & \sin 2\theta_1 \\ \sin 2\theta_1 & -\cos 2\theta_1 \end{bmatrix} \\ &\quad = \begin{bmatrix} \cos(4\theta_1 - 2Q) & \sin(4\theta_1 - 2Q) \\ -\sin(4\theta_1 - 2Q) & \cos(4\theta_1 - 2Q) \end{bmatrix} \\ &\quad = R'(4\theta_1 - 2Q). \end{aligned} \quad (6)$$

This is still a counter-rotation matrix $R'(4\theta_1 - 2Q)$, in which θ_1 and Q are the fast-axis direction of the VHP and QP, and $\theta_1 = m_1\varphi/2 + \varphi_{0,1}$, where $\varphi_{0,1}$ is the initial fast axis direction of VHP(θ_1) when $\varphi = 0$. So, when the Φ LP beam passes through the combined device above, the

corresponding Jones vector can be expressed as follows:

$$\begin{aligned} E_{\mathrm{ACV}}^{2m_1} &= R'(4\theta_1 - 2Q) \times E_{\Phi} \\ &= \begin{bmatrix} \cos(4\theta_1 - 2Q) & \sin(4\theta_1 - 2Q) \\ -\sin(4\theta_1 - 2Q) & \cos(4\theta_1 - 2Q) \end{bmatrix} \times \begin{bmatrix} \cos\Phi \\ \sin\Phi \end{bmatrix} \\ &= \begin{bmatrix} \cos(\Phi + 2Q - 2m_1\varphi - 4\varphi_{0,1}) \\ \sin(\Phi + 2Q - 2m_1\varphi - 4\varphi_{0,1}) \end{bmatrix} \\ &= \begin{bmatrix} \cos(-2m_1\varphi + \psi'_{0,1}) \\ \sin(-2m_1\varphi + \psi'_{0,1}) \end{bmatrix}. \end{aligned} \tag{7}$$

This is an antivortex cylindrical vector (ACV) beam [91] with the polarization order $P = -2m_1$ and initial polarization direction $\psi'_{0,1} = \Phi + 2Q - 4\varphi_{0,1}$ at $\varphi = 0$. So, $\psi'_{0,1}$ can be adjusted just by changing Q, i.e., rotating the QP(Q).

The counter-rotation matrix $R'(4\theta_1 - 2Q)$ can be converted to the function of a VHP when followed by a M or a 0 HP with the corresponding Jones matrix expressed as

$$J_M \times \Phi(4\theta_1 - 2Q) = \mathrm{e}^{i\pi} \times J_{\mathrm{VHP}}(2\theta_1 - Q). \tag{8}$$

This means an alternative VHP is formed with order number $m = 2m_1$ and initial fast-axis direction $\varphi_0 = 2\varphi_{0,1} - Q$. When it is passed through by the Φ LP beam, a CV beam with the polarization order $P = 2m_1$ and initial polarization direction $\psi_{0,1} = -\psi'_{0,1} = 4\varphi_{0,1} - 2Q - \Phi$ is obtained. So, the polarization order is doubled and multitype CV beams can be obtained just by rotating the QP(Q) or changing the initial polarization direction Φ of incident LP beam.

Besides, as it has been reported that the cascading of odd number $2n-1$ VHPs for $n \geq 1$ can form an alternative VHP with the order number $m = m_{2n-1} - m_{2n-2} + \ldots - m_2 + m_1$ [92]. Combined with the above-mentioned combination of Eqs. (6) and (8), multiple even-order CV beams can be obtained by multiplexing VHPs. When the combination of a HP and 1-order VHP is added after the last M, the odd- ($2m \pm 1$) order CV beams can be generated, including ACV beams when $m < 0$ adjusted by the position of cascaded odd VHPs. Thus, continuously adjustable CV beams can be obtained conveniently.

It is found that the cascading of even-number $2n$ VHPs can form the rotation function with the Jones matrix $R(2\Theta_{2n})$ [92], where $\Theta_{2n} = \theta_{2n} - \theta_{2n-1} + \ldots + \theta_2 - \theta_1$ and $\theta_{2n} = m_{2n}\varphi/2 + \varphi_{0,2n}$, in which θ_{2n} and $\varphi_{0,2n}$ represent the fast-axis and initial fast-axis direction of the $2n$-th VHP, respectively. Taking two VHPs for example, the combination of the VHP(θ_1), VHP(θ_2), a QP, and a M has the Jones matrix expressed as

$$\begin{aligned} &J_{\mathrm{VHP}}(-\theta_1) \times J_{\mathrm{VHP}}(-\theta_2) \times J_{\mathrm{QP}}(-Q) \times J_M \times J_{\mathrm{QP}}(Q) \\ &\quad \times J_{\mathrm{VHP}}(\theta_2) \times J_{\mathrm{VHP}}(\theta_1) \\ &\quad = R(-2\theta_1 + 2\theta_2) \times R'(2Q) \times R(2\theta_2 - 2\theta_1). \end{aligned} \tag{9}$$

That is to say, the Jones matrix of cascaded VHP(θ_1) and VHP(θ_2) in the opposite direction is still $R(2\theta_2 - 2\theta_1)$. By analogy, the combination of cascaded even VHPs, a QP, and a M can generate CV beams with the corresponding Jones matrix expressed as follows:

$$\begin{aligned} &R(2\Theta_{2n}) \times R'(2Q) \times R(2\Theta_{2n}) \\ &= \begin{bmatrix} \cos 2\Theta_{2n} & -\sin 2\Theta_{2n} \\ \sin 2\Theta_{2n} & \cos 2\Theta_{2n} \end{bmatrix} \times \begin{bmatrix} \cos 2Q & \sin 2Q \\ -\sin 2Q & \cos 2Q \end{bmatrix} \\ &\quad \times \begin{bmatrix} \cos 2\Theta_{2n} & -\sin 2\Theta_{2n} \\ \sin 2\Theta_{2n} & \cos 2\Theta_{2n} \end{bmatrix} \\ &= \begin{bmatrix} \cos(4\Theta_{2n} - 2Q) & -\sin(4\Theta_{2n} - 2Q) \\ \sin(4\Theta_{2n} - 2Q) & \cos(4\Theta_{2n} - 2Q) \end{bmatrix} \\ &= R(4\Theta_{2n} - 2Q). \end{aligned} \tag{10}$$

This is a rotation matrix with counterclockwise direction. When the Φ LP beam passes through the combination above, a CV beam with $P = 2(m_{2n} - m_{2n-1} + \ldots + m_2 - m_1)$ and initial polarization direction $\psi_{0,2n} = 4(\varphi_{0,2n} - \varphi_{0,2n-1} + \ldots + \varphi_{0,2} - \varphi_{0,1}) - 2Q + \Phi$ is obtained. If the combination is followed by a M or HP(0), a counter VHP is formed with the corresponding Jones matrix expressed as follows:

$$\begin{aligned} &J_M \times R(4\Theta_{2n} - 2Q) \\ &\quad = \begin{bmatrix} -\cos(4\Theta_{2n} - 2Q) & \sin(4\Theta_{2n} - 2Q) \\ \sin(4\Theta_{2n} - 2Q) & \cos(4\Theta_{2n} - 2Q) \end{bmatrix} \\ &\quad = J'_{\mathrm{VHP}}(2\Theta_{2n} - Q) = e^{i\pi} J_{\mathrm{VHP}}(Q - 2\Theta_{2n}). \end{aligned} \tag{11}$$

When the Φ LP beam pass through the combination above, an ACV beam with $P = -2(m_{2n} - m_{2n-1} + \ldots + m_2 - m_1)$ and initial polarization direction $\psi'_{0,2n} = -\psi_{0,2n} = -4(\varphi_{0,2n} - \varphi_{0,2n-1} + \ldots + \varphi_{0,2} - \varphi_{0,1}) + 2Q - \Phi$ is obtained. Also, CV beams can be generated when $P > 0$ adjusted by the position of cascaded even VHPs. And the odd- ($P \pm 1$) order CV beams can be captured when the combination of a HP and 1-order VHP is added before a CCD. Thus, multitype CV beams can be obtained either by rotating QP(Q) or changing the polarization direction Φ of incident beam by use of rotating a HP. Besides, the ACV and CV beam can be converted to each other by a M or HP(0). Therefore, continuously adjustable CV beams can be obtained combined with multiplexing and cascading skills.

C. Continuously adjustable vortex beams

When the 0 LP beam passes through the QP($\pi/4$) or QP($-\pi/4$), respectively, right-handed circularly polarized (RCP) or left-handed circularly polarized (LCP) beam will be obtained with the corresponding Jones vectors described as $E_R = \sqrt{2}/2\begin{bmatrix}1 & -\mathrm{i}\end{bmatrix}^T$ or $E_L = \sqrt{2}/2\begin{bmatrix}1 & \mathrm{i}\end{bmatrix}^T$. The VHP can transform incident circularly polarized beam into vortex wave front. When the RCP or LCP beam passes through the VHP(m, φ_0), the exit beam becomes a clockwise left-handed circularly polarized vortex (CLCV) beam or an anticlockwise right-handed circularly polarized vortex (ARCV) beam with the corresponding Jones vectors described as $E_{\mathrm{CLCV}} = E_L \times e^{-i(m\varphi+2\varphi_0)}$ or $E_{\mathrm{ARCV}} = E_R \times e^{i(m\varphi+2\varphi_0)}$ [91], in which $2\varphi_0$ is only an initial fixed phase and does not affect the relative phase distribution of the whole vortex beam.

According to Eq. (8), the alternative VHP($2m_1$, $2\varphi_{0,1} - \Phi/2 - Q$) can be formed with the combination of a VHP(m_1, $\varphi_{0,1}$), a QP(Q), and two mirrors. So, a circularly polarized (CP) vortex beam with doubled topological charge number $l = \pm 2m_1$ and initial phase $\sigma_0 = \pm(4\varphi_{0,1} - \Phi - 2Q)$ can be obtained by the combination mentioned above. Further, even high-order CP vortex beams can be generated by the combination of odd VHPs, a QP, and two mirrors, and odd ones are obtained when the combination of a HP and 1-order VHP is added after the second M.

Besides, according to Eq. (11), the combination of even VHPs, a QP, and two mirrors can form a counter VHP, which can convert the RCP beam to an anticlockwise left-handed circularly polarized vortex (ALCV) beam with the corresponding Jones vector expressed as follows:

$$\begin{aligned} &J_{\mathrm{VHP}}(Q - 2\Theta_{2n}) \times E_R \\ &= \begin{bmatrix} \cos(2Q - 4\Theta_{2n}) & \sin(2Q - 4\Theta_{2n}) \\ \sin(2Q - 4\Theta_{2n}) & -\cos(2Q - 4\Theta_{2n}) \end{bmatrix} \times \frac{\sqrt{2}}{2} \begin{bmatrix} 1 \\ -i \end{bmatrix} \\ &= e^{i(4\Theta_{2n} - 2Q)} \frac{\sqrt{2}}{2} \begin{bmatrix} 1 \\ i \end{bmatrix} = e^{i(l_{2n}\varphi + \sigma_{0,2n})} E_L. \end{aligned} \tag{12}$$

The generated ALCV beam has the topological charge $l_{2n} = 2(m_{2n} - m_{2n-1} + \ldots + m_2 - m_1)$ and initial phase $\sigma_{0,2n} = 4(\varphi_{0,2n} - \varphi_{0,2n-1} + \ldots + \varphi_{0,2} - \varphi_{0,1}) - 2Q$. And the initial phase $\sigma_{0,2n}$ can be modulated by rotating QP(Q). Also, the combination above can convert a LCP beam to a clockwise right-handed circularly polarized vortex (CRCV) beam with the corresponding Jones vector $J_{\mathrm{VHP}}(Q - 2\Theta_{2n}) \times E_L = e^{-i(l_{2n}\varphi + \sigma_{0,2n})} E_R$. So, positive topological charge l can be converted to a negative one by changing the sequence of VHPs or the polarization state of the incident beam. And odd vortex beams can be obtained with the combination of a HP and 1-order VHP added. Thus, continuously adjustable vortex beams can be obtained combined with multiplexing and cascading VHPs.

D. Coaxial and small-angle interference

It is assumed that both Gaussian plane wave and vortex beam are horizontally polarized. At the same time, assuming that all beams propagate in the x-z plane and the angles between the propagation direction of Gaussian plane wave, vortex beam, and CV beam and z axis are α, β, and γ changing from $-\pi/2$ to $\pi/2$, respectively, in which counterclockwise angles traced from the incident ray to z axis have positive sign, and clockwise angles have negative sign. The complex amplitudes of Gaussian plane wave, vortex beam, and CV beam at $z = 0$ observation plane can be expressed as

$$\begin{aligned} U_G &= A(r) e^{ikx \sin\alpha}, \\ U_V &= A(r) e^{i(l\varphi + \sigma_0)} e^{ikx \sin\beta}, \\ U_{\mathrm{CV\_}x} &= A(r) \cos(P\varphi + 2\varphi_0) e^{ikx \sin\gamma}, \\ U_{\mathrm{CV\_}y} &= A(r) \sin(P\varphi + 2\varphi_0) e^{ikx \sin\gamma}, \end{aligned} \tag{13}$$

where $A(r) = A_0 e^{-r^2/\omega_0^2}$ represents the amplitude distribution of Gaussian beam, in which A_0 is a constant, r is a variable representing the beam radius, and ω_0 is the beam waist radius. k is the wave vector with $k = 2\pi/\lambda$, l and σ_0 are the topological charge number and initial phase of vortex beam, respectively. U_{CV_x} and U_{CV_y} are the horizontal-polarization and vertical-polarization complex amplitude of CV beam, respectively. P and $2\varphi_0$ are the polarization order number and initial polarization direction of CV beam.

The interference intensity distribution between Gaussian plane wave and vortex beam can be expressed as

$$\begin{aligned} I_{G\_V} &= (U_G + U_V)(U_G + U_V)^* \\ &= A^2(r)(e^{ikx \sin\alpha} + e^{i(l\varphi + \sigma_0)} e^{ikx \sin\beta}) \\ &\quad \times (e^{-ikx \sin\alpha} + e^{-i(l\varphi + \sigma_0)} e^{-ikx \sin\beta}) \\ &= A^2(r)\{2 + 2\cos[kx(\sin\alpha - \sin\beta) - (l\varphi + \sigma_0)]\}. \end{aligned} \tag{14}$$

When $l = 0$, it means the interference of two Gaussian plane beams. The interference intensity distribution is vertical fringes, and the fringe spacing is $\Delta d = 2\pi/(k|\sin\alpha - \sin\beta|) = \lambda/|\sin\alpha - \sin\beta|$. The smaller the angle between α and β, the greater the fringe spacing Δd. When the incident angle $\alpha = \beta$, the interference intensity distribution is fan shaped. The number of fan-shape regions is positively correlated with the absolute value of topological charge l, and the fan-shaped orientation is related to initial phase σ_0. For the general case of $l \neq 0$ and $\alpha \neq \beta$, it is discussed in Sec. IV.

The interference intensity distribution of two vortex beams can be expressed as

$$\begin{aligned} I_{V1\_V2} &= (U_{V1} + U_{V2})(U_{V1} + U_{V2})^* \\ &= A^2(r)(e^{i(l_1\varphi+\sigma_{01})}e^{ikx\sin\beta_1} + e^{i(l_2\varphi+\sigma_{02})}e^{ikx\sin\beta_2}) \\ &\quad \times (e^{-i(l_1\varphi+\sigma_{01})}e^{-ikx\sin\beta_1} + e^{-i(l_2\varphi+\sigma_{02})}e^{-ikx\sin\beta_2}) \\ &= A^2(r)\{2 + 2\cos[(l_1 - l_2)\varphi + (\sigma_{01} - \sigma_{02}) \\ &\quad + kx(\sin\alpha - \sin\beta)\}. \end{aligned} \tag{15}$$

It has a similar law with the interference between Gaussian plane wave and vortex beams, where l and σ_0 are replaced by $l_1 - l_2$ and $\sigma_{01} - \sigma_{02}$, respectively.

The interference intensity between Gaussian plane wave and CV beams can be expressed as

$$\begin{aligned} I_{G\_CV} &= (U_G + U_{CV\_x})(U_G + U_{CV\_x})^* + U_{CV\_y}U_{CV\_x}^* \\ &= A^2(r)(e^{ikx\sin\alpha} + \cos(P\varphi + 2\varphi_0)e^{ikx\sin\gamma}) \\ &\quad \times (e^{-ikx\sin\alpha} + \cos(P\varphi + 2\varphi_0)e^{-ikx\sin\gamma}) \\ &\quad + A^2(r)\sin^2(P\varphi + 2\varphi_0) \\ &= A^2(r)\{2 + 2\cos(P\varphi + 2\varphi_0) \\ &\quad \times \cos[kx(\sin\alpha - \sin\gamma)]\}. \end{aligned} \tag{16}$$

When $P = 0$, it means the interference of 0 LP and $2\varphi_0$ LP Gaussian beams. The interference intensity distribution is still vertical fringes with the fringe spacing $\Delta d = \lambda/|\sin\alpha - \sin\gamma|$ but with an overall beam intensity base $2A^2(r)(1 - \cos 2\varphi_0)$, which is the intensity at the darkest fringes. When the incident angle $\alpha = \gamma$, fan-shaped intensity distribution appears with partition number $N = |P|$. For the general case of $P \neq 0$ and $\alpha \neq \gamma$, it is discussed in Sec. IV.

However, without considering propagation distance L and diffraction effect, the above conclusions can only point out the approximate and partial interference laws. More accurate complex amplitudes at z observation distance need to consider the Fresnel diffraction under paraxial approximation with the expressions as follows:

$$\begin{aligned} U_G(x,y,z) &= \frac{A_0 e^{ikz}}{i\lambda z}\iint e^{-(x'^2+y'^2)/\omega_0^2} e^{(ik/2z)[(x-x')^2+(y-y')]^2} dx'dy' \times e^{ikx\sin\alpha}, \\ U_V(x,y,z) &= \frac{A_0 e^{ikz}}{i\lambda z}\iint e^{-(x'^2+y'^2)/\omega_0^2} e^{i(l\times a\tan\frac{y'}{x'}+\sigma_0)} e^{(ik/2z)[(x-x')^2+(y-y')]^2} dx'dy' \times e^{ikx\sin\beta}, \\ U_{CV\_x}(x,y,z) &= \frac{A_0 e^{ikz}}{i\lambda z}\iint e^{-(x'^2+y'^2)/\omega_0^2} \cos\left(P \times a\tan\frac{y'}{x'} + 2\varphi_0\right) e^{(ik/2z)[(x-x')^2+(y-y')]^2} dx'dy' \times e^{ikx\sin\gamma}, \\ U_{CV\_y}(x,y,z) &= \frac{A_0 e^{ikz}}{i\lambda z}\iint e^{-(x'^2+y'^2)/\omega_0^2} \sin\left(P \times a\tan\frac{y'}{x'} + 2\varphi_0\right) e^{(ik/2z)[(x-x')^2+(y-y')]^2} dx'dy' \times e^{ikx\sin\gamma}. \end{aligned} \tag{17}$$

Thus, more detailed interference laws at $z = L$ observation plane can be obtained.

III. EXPERIMENTAL SETUP

A concise and versatile experimental setup for doubling the order of CV beam and vortex beam by multiplexing VHP is shown in Fig. 1 when there are no components in the black dashed line. The incident beam from a LP He-Ne laser is expanded 6 times by a beam expander (BE). The combination of a HP and a horizontal polarizer can both modulate the incident beam intensity and ensure the incident beam is horizontally linearly polarized. A NPBS divides a beam into two beams equally, one of which is the transmitted beam and the other is the reflected beam. In the setup, the NPBS is used twice, the first time it is transparent for the transmitted beam, and mirror 1 (M1) is used to reflect the transmitted beam back vertically. And the second time the NPBS corresponds to the function of a mirror. The reflected beam is captured by a CCD camera

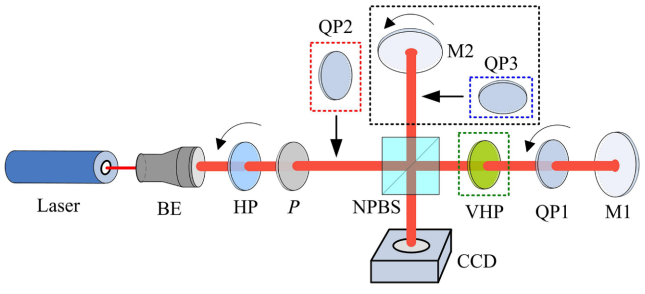

FIG. 1. Experimental setup for doubling and detecting the order of CV and vortex beam. BE, beam expander; HP, half-wave plate; *P*, polarizer; NPBS, nonpolarized beam splitter; VHP, vortex half-wave plate; QP, quarter-wave plate; *M*, mirror.

with the resolution of 1024×1024 pixels and pixel pitch 5.5×5.5 μm.

According to Eq. (6), the combination of a VHP, a QP1 and a mirror (M1) can form the function of counter rotation matrix $R'(4\theta_1 - 2Q)$, in which $\theta_1 = m_1\varphi/2 + \varphi_{01}$ and Q are the fast-axis direction of VHP and QP1, respectively. The initial fast-axis direction of the VHP is modulated to $\varphi_{01} = 0$. As mentioned above, the second use of NPBS is equivalent to a mirror. According to Eq. (8), the $R'(4\theta_1 - 2Q)$ is converted to the VHP$(2\theta_1 - Q)$ by the NPBS. So, a $2m_1$-order CV beam with the initial polarization direction $\psi_0 = -2Q$ can be generated by the setup for the incident beam with horizontal linear polarization. By simply rotating the QP1 to change Q, multitype CV beams can be obtained, including high-order radially polarized (RP) and azimuthally polarized (AP) beam. Besides, the VHP in the green dashed line can be replaced by cascaded odd VHPs to generate adjustable doubled high-order CV beams without changing other devices of the setup. In addition, when the combination of a HP and 1-order VHP is added before the CCD, the odd-order CV beams can be generated. Thus, the continuously adjustable CV beams are obtained. According to Eqs. (10) and (11), when the VHP is replaced by cascaded even VHPs, the CCD will capture an ACV beam, and multiple type can be realized by rotating the QP1. Moreover, the ACV beam can be converted to the CV beam when a 0 HP is placed between the NPBS and CCD, or the 0 HP is added into the even VHPs to form odd VHPs.

When the second QP (QP2) in the red dashed line with the fast axis orientated at 45° or −45° is inserted in the setup, a CLCV beam with doubled topological charge number $l = -2m_1$ or an ARCV beam with $l = 2m_1$ can be obtained. Similarly, adjustable high-order vortex beams can be generated by cascading odd VHPs instead of the VHP in the setup. While for cascaded even VHPs, according to Eq. (12), the RCP or LCP beam can be converted to the anticlockwise left-handed circularly polarized vortex (ALCV) beam with $l_{2n} = 2(m_{2n} - m_{2n-1} + \ldots + m_2 - m_1)$ or $(-l_{2n})$-order CRCV beam, respectively. Anyway, the incident beam and the exit beam have completely complementary polarization and cannot interfere with each other.

In order to detect the order of CV or vortex beam conveniently, the elements in the black dashed line need to be inserted. For the interference of Gaussian wave and CV beam, only M2 needs to be added. The interference angle can be adjusted by rotating M2. While for the vortex beam, the QP2 in the red dashed line and QP3 with the fast axis orientated at 45° or −45° in the blue dashed line are also needed to be inserted in the same time. Taking QP2$(-\pi/4)$ and QP3$(\pi/4)$ for instance, the generated LCP beam is divided into two parts by the NPBS. The transmitted part passes through the VHP$(m_1, 0)$ and QP1(Q), then is reflected by the M1. The CCD will capture the ARCV beam with topological charge $l = 2m_1$ and the initial phase $\sigma_0 = -2Q$. The reflected one passes through the QP3$(\pi/4)$ and is reflected by the M2. According to Eq. (4), the LCP beam is converted to RCP beam with corresponding Jones vortex expressed as $J_{QP}(-\pi/4) \times J_M \times J_{QP}(\pi/4) \times J_M \times E_L = e^{-i\pi/2} \times E_R$. Then, the RCP Gaussian beam and vortex beam can interference with each other in the CCD. The incident angle α of Gaussian beam can be modulated by rotating M2. When rotating or reversing the QP2$(-\pi/4)$ to QP2$(\pi/4)$, the $(-2m_1)$-order CLCV beam will be obtained. In order to simplify the experiment, the M1 is fixed and ensures the beam is reflected vertically, i.e., the incident angle β or γ of vortex or CV beam are both 0. Thus, the angle of two interference beams is adjusted only by M2, i.e., adjusting α. For coaxial interference, α is adjust to be 0, and for small-angle interference, positive α is researched experimentally, while the opposite laws will be obtained when $\alpha < 0$.

IV. RESULTS AND DISCUSSION

In the experiment, the VHPs with $m = 1$, 3, and 8 are used to generate −24 to 24-order CV and vortex beams combined with doubling and cascading skills. Figure 2 shows the generated 16-order RP (16-RP for short), (−17)-order AP (−17-AP for short), and 24-order CV (24-CV for short) beam by multiplexing a VHP(8, 0), a single VHP(1, 0) and multiplexing a VHP(8, 0), and multiplexing the cascading of VHPs$(m, 0)$ with $m = 1$, 3, and 8, respectively. Figures 2(a1)–2(c1) are the whole intensity distributions, respectively, i.e., I_0. It is clear that the bright ring in Fig. 2(c1) is larger due to the higher order. And

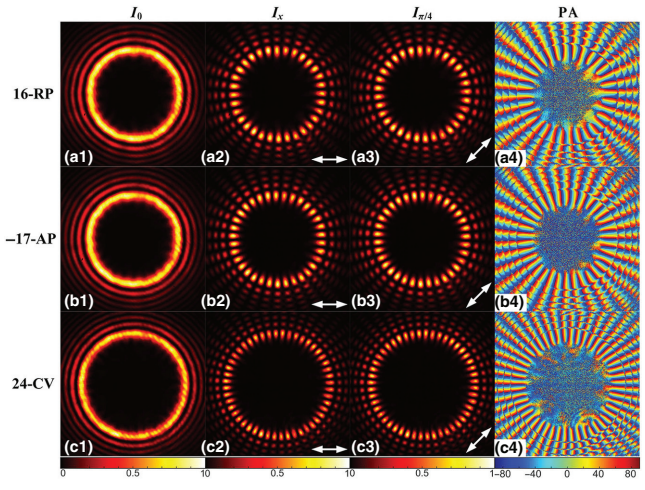

FIG. 2. Intensity and polarization azimuth distributions of generated 16-RP, −17-AP and 24-CV beams. (a) 16-RP beam; (b) −17-AP beam; (c) 24-CV beam; (1–4): I_0, I_x, I_y, and PA. Two-way arrowheads indicate the transmission direction of a polarizer.

Figs. 2(a2)–2(c3) are the intensity distributions after passing through a linear polarizer with the polarization direction orientated at 0° and 45°, respectively, i.e., I_x and I_y. It can be found that the number of intensity divisions are 32, 34, and 48, respectively, which are twice the order values. All intensity distributions of I_0, I_x, and I_y are normalized. RP or AP beam can be obtained by rotating QP1 in the experimental setup. The corresponding PA distributions are depicted in Figs. 2(a4)–2(c4) calculated by measured Stokes parameters. For positive-order CV beams, the rotation direction from red (90°) to adjacent blue (−90°) in PA is counterclockwise, such as Figs. 2(a4) and 2(c4), while for negative order ones, the rotation direction becomes clockwise, as shown in Fig. 2(b4). Both the polarization order and polarization direction can be identified from the PA.

According to Sec. II D, the order numbers of vortex and CV beams can be detected by the interference with Gaussian plane beam. For the coaxial interference with the incident angle $\alpha = \beta$ by adjusting M2, the simulated interference results are shown in Fig. 3. Figures 3(a1)–3(a5) are the intensity distributions of vortex beams with $l = 1$, 2, 3, 4, and 6, and Figs. 3(b1)–3(b5) are for vortex beams with $l = -1$, -2, -3, -4, and -6. It is found that the interference intensity distribution is spirally fan shaped, and the number N of fan-shape regions equals the absolute value of topological charge l, i.e., $N = |l|$. Besides, the fan-shaped orientation is decided by the initial phase σ_0, which can be adjusted by changing the fast axis of QP1, i.e., rotating QP1. In addition, the spiral direction from the outer tail to center head of fan-shape regions in the central part is related to the sign of l. For positive l, the spiral direction is counterclockwise, and the negative one has clockwise direction, which is caused by the different divergence angles of vortex beams with different orders.

As it is known that the higher the order value of the vortex beam, the larger the dark area in the center and the more outward the bright ring at the same observation distance. That is, the higher the order value, the greater the divergence angle. Take the 1-order vortex beam for example

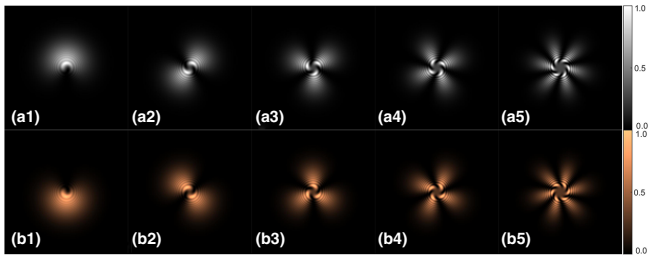

FIG. 3. Simulated interference intensity distributions between vortex and Gaussian plane beams at $\alpha = \beta$. (a1)–(a5) Vortex beams with $l = 1$, 2, 3, 4, and 6; (b1)–(b5) vortex beams with $l = -1$, -2, -3, -4, and -6.

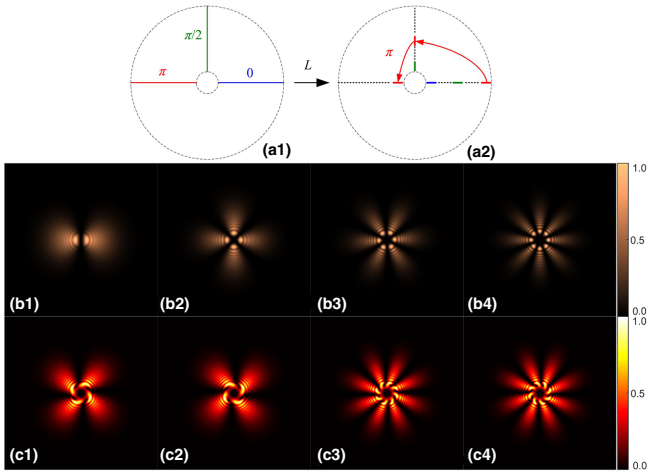

FIG. 4. Sketch of vortex beam phase diffraction distribution and simulated interference intensity distributions between vortex beams at $\alpha = \beta$. (a1)–(a2) Sketch of partial phase distribution of 1-order vortex beam at $z = 0$ and $z = L$; (b1)–(b4) interference of conjugate vortex beams with $l = \pm 1$, ± 2, ± 3, and ± 4, respectively; (c1)–(c4) interference of 2- and 6-, -2- and -6-, -2- and 6-, and 2- and -6-order vortex beams, respectively.

as shown in Fig. 4. Figure 4(a1) shows the partial initial phase distribution at $z = 0$, in which the blue line represents 0 phase, green and red lines represent $\pi/2$ and π phase, respectively. Due to the influence of diffraction and divergence angle, the farther away from the center, the greater the propagation distance, and thus the more phase delay. Therefore, on the observation plane perpendicular to the propagation direction, the phase distribution of the same azimuth is no longer consistent. The phase distribution sketch at $z = L$ is shown in Fig. 4(a2), where the π isophase line is shown with the red curve, and the arrow direction is from the outer tail to the central head, which is counterclockwise for positive order. However, for negative-order vortex beams, the phase direction becomes clockwise, and the isophase line changes accordingly. The phase change of the Gaussian beam relative to the high-order vortex beam is small. When the two interfere with each other, it can be approximated that the phase of the Gaussian beam does not change and the whole is in phase. Therefore, the distribution of the interference intensity will be consistent with the isophase line distribution of the vortex beam. Thus, the reason for the spiral fan-shaped intensity distribution in Fig. 3 and the relationship with the order sign of the vortex beam are qualitatively explained.

Since the conjugate vortex beams with the same order value $|l|$ and opposite sign have the same divergence angle, the phase distribution at the same propagation distance is relatively unchanged. Therefore, when they interfere with each other coaxially, the spiral intensity distribution will not appear, and the partition number is $N = 2|l|$, as shown

in Fig. 4(b). Figures 4(b1)–4(b4) are the interference intensity distributions of conjugate vortex beams with $l = \pm 1$, ± 2, ± 3 and ± 4, respectively. Furthermore, for the coaxial interference between l_1-order and l_2-order vortex beams, the intensity spiral distribution will be consistent with the isophase line direction of vortex beam with higher value, and the partition number is $N = |l_2 - l_1|$. The coaxial interference between ± 2- and ± 6-order vortex beams are shown in Fig. 4(c). Figure 4(c1) is for the interference of 2- and 6-order vortex beams, and Figs. 4(c2)–4(c4) are for -2- and -6-, -2- and 6-, and 2- and -6-order vortex beams, respectively. It can be found that the spiral direction of the interference intensity is determined by the isophase line of the (± 6)-order vortex beam, and partition number N equals 4 or 8, which is the absolute value of the order difference. The quantitative simulation results are completely consistent with the qualitative analysis.

Figure 5 shows the experimental coaxial interference between Gaussian plane beam and generated 2-order, 4-order, and 6-order vortex beams with the VHP(1,0) and VHP (3,0). Figures 5(a1)–5(a3) are the intensity distributions of vortex beams with $l = 2$, 4, and 6. The intensity spiral direction from the outer tail to center head is counterclockwise for positive order, and the partition number is $N = l$. And Figs. 5(b1)–5(b3) are for vortex beams with $l = -2$, -4, and -6. The intensity spiral direction is clockwise with partition number $N = -l = |l|$. Comparing Figs. 5(a1) and 5(b1), Figs. 5(a4) and 5(b4) are other 2-order and (-2)-order vortex beams with different initial phase σ_0 adjusted by rotating QP1. It can be found that the experimental results are greatly consistent with the theoretical simulation ones.

When the incident angle $\alpha > 0$ by adjusting M2, the simulated interference results with $\beta = 0$ are shown in Fig. 6. Figures 6(a1)–6(a5) are the interference fringe distributions of vortex beams with $l = 1$, 2, 3, 4, and 6, and Figs. 6(b1)–6(b5) are for $l = -1$, -2, -3, -4, and -6. The

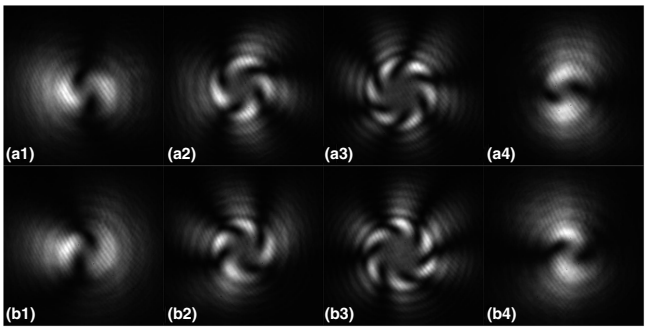

FIG. 5. Experimental interference intensity distributions between vortex and Gaussian plane beams at $\alpha = \beta = 0$. (a1)–(a3) Vortex beams with $l = 2$, 4, and 6; (b1)–(b3) vortex beams with $l = -2$, -4, and -6; (a4)–(b4) 2-order and (-2)-order vortex beam with different initial phase σ_0.

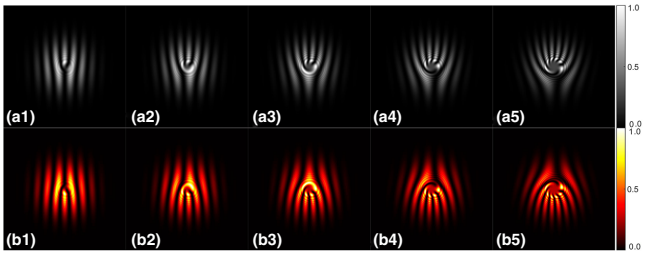

FIG. 6. Simulated interference fringe distributions between vortex and Gaussian plane beams at $\alpha > 0$ and $\beta = 0$. (a1)–(a5) Vortex beams with $l = 1$, 2, 3, 4, and 6; (b1)–(b5) vortex beams with $l = -1$, -2, -3, -4, and -6.

fringe spacing can be adjusted by changing the angle value between α and β. It is found that the fringes are no longer vertical and bifurcate in the central region, and the forking number N between two fringes equals the value of l, i.e., $N = |l|$, such as Figs. 6(a1), 6(a4), and 6(a5), or the forking number from a single fringe is equal to $|l| + 1$, such as Figs. 6(a2) and 6(a3). In actual fact, both have the same connotation. When an adjacent fringe is merged into the latter, it becomes the former. For the sake of unification, we choose the expression of the former.

It is found that the fork faces upward or downward for positive or negative l, respectively, and the different relative forking distributions are caused by the initial phase σ_0 of vortex beam, or relative position of Gaussian plane and vortex beams. Taking the (± 1)-order vortex beam as an example, Fig. 7 depicts the causes clearly. Figure 7(a) displays the isophase line distribution when a Gaussian beam is incident on the observation plane at $\alpha > 0$. It could be found that the phase increases continuously along the direction of the arrow. Select one of the phases as the origin 0 to establish the phase coordinates of the Gaussian beam, expressed in x. Figure 7(b) depicts the small-angle interference intensity distribution between Gaussian plan beam and 1-order vortex beam with $\sigma_0 = 0$. The green vertical dashed line represents the isophase line x of the Gaussian beam, and the blue dashed line depicts the isophase line of the vortex beam, expressed in θ $(2\pi > \theta \geq 0)$. The red curves show the interference fringe distribution when the center of vortex beam coincides with the coordinate origin 0 of Gaussian beam, where the Gaussian and vortex beam have the same phase, that is,

$$\theta = x + 2n\pi \quad (n = 0, \pm 1, \pm 2 \ldots), \tag{18}$$

which is in consideration of the periodicity of the phase. Taking the coordinates (θ, x) of the four points marked on the red curves as an example, the coordinates of (1–4) are $(\pi/4,\ \pi/4)$, $(3\pi/4,\ -5\pi/4)$, $(5\pi/4,\ -19\pi/4)$, and $(7\pi/4,\ 15\pi/4)$, respectively. The red curves depict the forking orientation, the relative forking distribution and forking

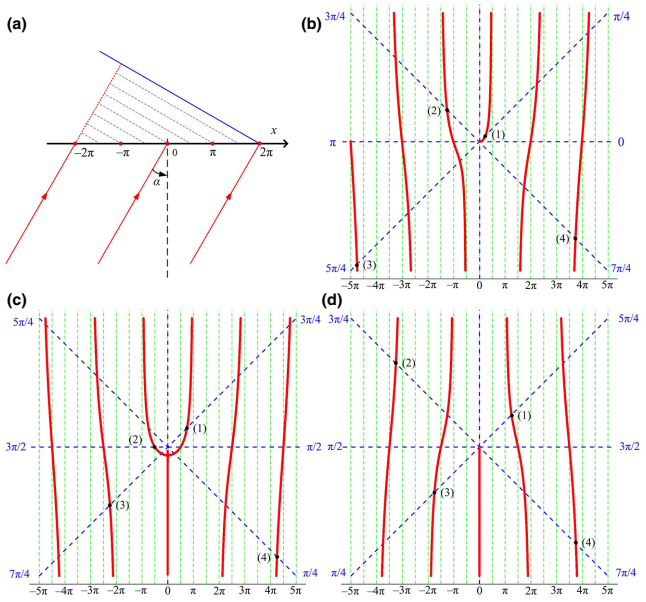

FIG. 7. Sketch of isophase line distribution of Gaussian plane beam and small-angle interference intensity distribution of Gaussian plane and (±1)-order vortex beam with different σ_0. (a) Isophase line distribution of Gaussian beam at $\alpha > 0$; (b),(c) interference fringe distribution between Gaussian plane and 1-order vortex beam with $\sigma_0 = 0$ and $\pi/2$, respectively; (d) interference fringe distribution between Gaussian plane and (−1)-order vortex beam with $\sigma_0 = 3\pi/2$.

number N, i.e., the fork faces upward and the forking number between two fringes satisfies $N = |1 - 0| = 1$, which is the value of the order difference between Gaussian and vortex beams.

Similarly, the red curves in Fig. 7(c) show the interference results for 1-order vortex beam with $\sigma_0 = \pi/2$. The coordinates of (1–4) from the red curves meeting Eq. (18) are $(3\pi/4, 3\pi/4)$, $(3\pi/2, -\pi/2)$, $(7\pi/4, -9\pi/4)$, and $(7\pi/4, 15\pi/4)$, respectively. It is clear that the forking orientation does not change, but the relative forking distribution becomes a single fringe bifurcating and forking number $N = |1 - 0| + 1 = 2$. When an adjacent fringe is included, it could be considered that the forking number between two fringes still meets $N = |1 - 0| = 1$. Therefore, the initial phase σ_0 of vortex beam could affect the relative forking distribution. Furthermore, the change of relative position of Gaussian plane and vortex beams also affects the relative forking distribution. When the center of 1-order vortex beam with $\sigma_0 = \pi/2$ coincides with the coordinate $\pi/2$ of Gaussian beam, the interference fringe distribution will be consistent with the red curves in Fig. 7(b). Also, the fringe distribution will change into the red curves in Fig. 7(c) when the center of 1-order vortex beam with $\sigma_0 = 0$ coincides with the coordinate $-\pi/2$ of Gaussian beam. Figure 7(d) depicts the interference fringe distribution for (−1)-order vortex beam with $\sigma_0 = 3\pi/2$. (1–4) points out of red curves satisfying Eq. (18) are $(5\pi/4, 5\pi/4)$, $(3\pi/4, -13\pi/4)$, $(\pi/4, -7\pi/4)$, and $(7\pi/4, 15\pi/4)$, respectively. Clearly, the fork faces downward for negative l, and the law of the relative forking distribution and forking number does not change. Significantly, when the Gaussian plane beam incidences at $\alpha < 0$, the phase coordinates will change to decrease continuously along the arrow direction. Thus, the forking orientation change to be downward or upward for positive or negative l, respectively, and the forking number between two fringes still satisfies $N = |l - 0| = |l|$.

More generally, for the small-angle interference of l_1-order and l_2-order vortex beams with incident angle β_1 and β_2, respectively, the forks face upward when $l_1 < l_2$ & $\beta_1 > \beta_2$ (l_1-order vortex beam lies the left of l_2-order one), or $l_1 > l_2$ & $\beta_1 < \beta_2$ (l_1-order vortex beam lies the right of l_2-order one), i.e., $(l_2 - l_1) \times (\beta_2 - \beta_1) < 0$, and the forks face downward when $l_1 > l_2$ and $\beta_1 > \beta_2$, or $l_1 < l_2$ & $\beta_1 < \beta_2$, i.e., $(l_2 - l_1) \times (\beta_2 - \beta_1) > 0$. And the forking number between two fringes always meets $N = |l_2 - l_1|$, and the greater the value of the relative included angle $|\beta_2 - \beta_1|$, the narrower the fringe spacing. Besides, considering beam diffraction and divergence angle, the intensity fringes rotate clockwise or anticlockwise from the outer to center at the bifurcation near the center, which is determined by the sign of the higher absolute value of l. The interference fringe distributions between vortex beams with different l and β are shown in Fig. 8. Figures 8(a1) and 8(a3) are the results of conjugate vortex beams with $l = \pm 1$ roughly interchanging relative incident angle. The forks face upward for $(l_2 - l_1) \times (\beta_2 - \beta_1) < 0$, and face downward for $(l_2 - l_1) \times (\beta_2 - \beta_1) > 0$. The forking number $N = |l_2 - l_1| = 2$, and the fringe spacing in Fig. 8(a3) is narrower than the one in Fig. 8(a1) due to the greater $|\beta_2 - \beta_1|$. Due to $|l_1| = |l_2|$, there is no fringe

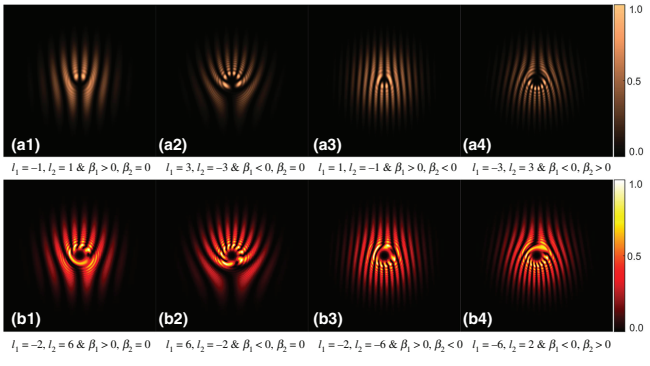

FIG. 8. Simulated interference fringe distributions between vortex beams with different l and β. (a) Interference of conjugate vortex beams with $l = \pm 1, \pm 3$ in different relative included angle $(\beta_2 - \beta_1)$; (b) interference of nonconjugate vortex beams with $l = \pm 2, \pm 6$ in different relative included angle $(\beta_2 - \beta_1)$.

rotation at the bifurcation near the center. The similar patterns show in Figs. 8(a2) and 8(a4) with $N = |l_2 - l_1| = 6$ for conjugate (± 3)-order vortex beams. Figures 8(b1) and 8(b2) display the results between ± 2- and 6-order vortex beams and forks face upward due to $(l_2 - l_1) \times (\beta_2 - \beta_1) < 0$, and N is $|6 - 2| = 4$ and $|6 - (-2)| = 8$, respectively. Besides, it is found that the forking fringes rotate anticlockwise from the outer to center at the bifurcation near the center because of positive 6 as the higher-order value. Figures 8(b3) and 8(b4) are results with narrower fringe spacing for ∓ 2- and -6-order vortex beams in greater $|\beta_2 - \beta_1|$, and forks face downward due to $(l_2 - l_1) \times (\beta_2 - \beta_1) > 0$ and N between two adjacent fringes is $|-6 - (-2)| = 4$ and $|-6 - 2| = 8$, respectively. And the forking fringes rotate clockwise because of negative 6 as the higher-order value.

The small-angle interference results between generated (± 2)-order, (± 4)-order, and (± 6)-order vortex and Gaussian plane beams at $\alpha > 0$ are shown in Fig. 9. Figures 9(a1)–9(a3) and 9(b1)–9(b3) are the interference fringe distributions of vortex beams with $l = 2$, 4, 6 and $l = -2$, -4, -6, respectively. The forks face upward or downward for $l > 0$ or $l < 0$, respectively. And the forking number between two fringes satisfies $N = |l|$. Compared with Figs. 9(a1), 9(a3), 9(b1) and 9(b3), Figs. 9(a4)–9(b5) are other $l = 2$, 6 and $l = -2$, -6 vortex beams with different initial phase σ_0 adjusted by rotating QP1. The relative forking distribution change into a single fringe bifurcating, and the forking number from a single fringe meets $N = |l| + 1$. Besides, the forking fringes rotate anticlockwise or clockwise from the outer to center at the bifurcation near the center for positive or negative topological charge l. So, it is not like they are upside down. And the higher the order value, the more obvious the rotation. It is clear that the experimental results are in very good agreement with the theoretical simulation ones.

The simulated interference between Gaussian plane beam and CV beams is shown in Fig. 10. Figures 10(a1)–10(a5) are the interference intensity distributions for CV

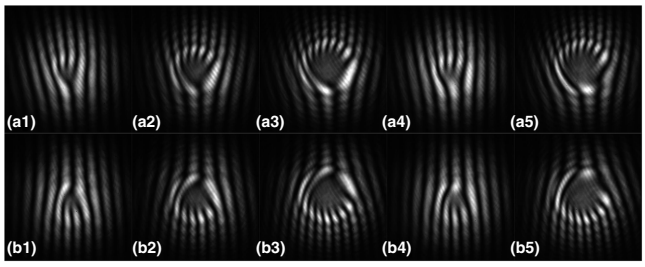

FIG. 9. Experimental interference fringe distributions between vortex and Gaussian plane beams at $\alpha > 0$. (a1)–(b3) Vortex beams with $l = 2$, 4, 6 and $l = -2$, -4, -6, respectively; (a4)–(b5) $l = 2$-, 6- and $l = -2$-, -6-order vortex beams with different initial phase σ_0.

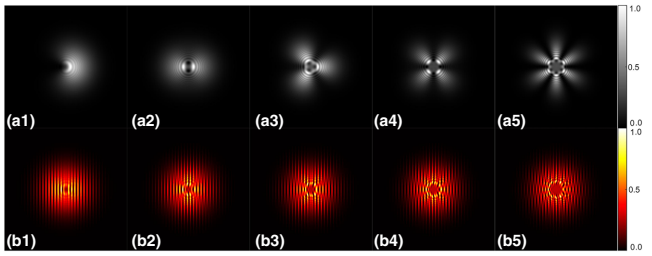

FIG. 10. Simulated interference intensity distributions between Gaussian plane beam and CV beams. (a),(b) $\alpha = \gamma$, $\alpha \neq \gamma$; (1–5): $P = 1$, 2, 3, 4, and 6.

beams with the polarization order $P = 1$, 2, 3, 4, and 6 when $\alpha = \gamma$, in which fan-shaped partition is formed. And Figs. 10(b1)–10(b5) are the corresponding results at $\alpha \neq \gamma$, in which vertical fringes appear misplaced and partitioned. It is found that the number N of interference intensity partitions is equal to $|P|$ and $2|P|$ for $\alpha = \gamma$ and $\alpha \neq \gamma$, respectively. And positive and negative P have the similar interference results, which can be distinguished by measured PA.

The corresponding experimental interference results of CV beams are shown in Fig. 11. Figures 11(a1)–11(a3) and 11(b1)–11(b3) are the interference intensity distributions of CV beams with $P = 2$, 4, and 6 for $\alpha = \gamma = 0$ and $\alpha \neq 0$, respectively. The partition number N of coaxial and small-angle interference intensity equals 2, 4, 6 and 4, 8, 12, respectively. Comparing Figs. 11(a1), 11(a3), 11(b1) and 11(b3), Figs. 11(a4)–11(b5) are the other $P = 2$, 6 CV beams with different initial phase ψ_0 adjusted by rotating QP1, clearly the relative intensity distribution orientations change. For small-angle interference, due to the small spot size and limited interference area, the experimental interference phenomena for high-order CV beams are not very clear, but it is still very consistent with the theoretical simulation results through careful identification. The issue can be improved by expanding the spot with larger size. The experimental results accord with the theoretical simulation ones well. The advantage of this identification method is

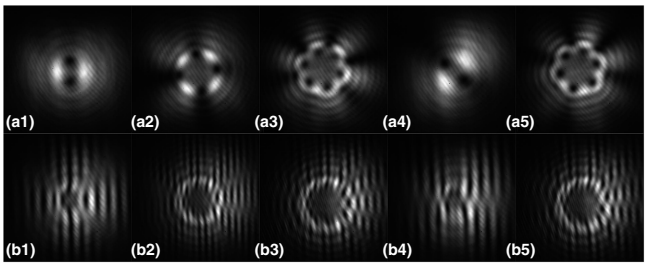

FIG. 11. Experimental interference intensity distributions between Gaussian plane beam and CV beams. (a),(b) $\alpha = 0$, $\alpha \neq 0$; (1–3) CV beams with $P = 2$, 4 and 6; (4–5): other CV beams with $P = 2$ and 6 with different initial phase ψ_0.

that the polarization order can be identified quickly without the help of other optical devices, including polarizer.

In addition, comparing the coaxial interference and small-angle interference, the latter has better stability and operability. However, when the spot size is relatively small or the order is a little high, coaxial interference will be more practical. Further, the adjusting of initial phase σ_0 of vortex beam just by rotating the QP1 is expected to be applied in phase retrieval and measuring the surface topography of objects by four-step phase shift. Generally, the phase shift is realized by precise PZT, stepping motor, or SLM. In comparison, the method of rotating a QP will be a more economical and practical choice.

V. CONCLUSION

In summary, we demonstrate a convenient scheme to double the order of CV and vortex beam by multiplexing the passive VHP. The principle of doubling skill is introduced in detail. Combined with cascading technology, continuous (-24)- to 24-order CV and vortex beams are generated by use of VHPs with order number $m = 1$, 3, and 8, and the PA distributions of generated CV beams are investigated by measured Stokes parameters. Besides, the coaxial interference and small-angle interference are introduced to detect the order of vortex and CV beams. There is only a NPBS in the proposed scheme, which simplifies the system complexity and improves the energy utilization. For vortex beams, both the value and sign of topological charge l can be detected by the interference conveniently. While, the interference between Gaussian plane beam and CV beams can only detect the value of polarization order P, but the sign can be identified by measured PA. The advantage is that the polarization order can be identified quickly without the help of other optical devices, including polarizer. Further, the initial phase σ_0 of vortex beams and multitype CV beams can be easily adjusted only by rotating a quarter-wave plate. In particular, the adjusting of initial phase σ_0 is expected to be applied in phase retrieval and measuring the surface topography of objects by four-step phase shift. It is experimentally demonstrated that the proposed scheme can effectively generate continuously adjustable CV and vortex beams with limited VHPs, which can greatly expand the order numbers with low cost, low energy consumption and high utilization, and the coaxial and small-angle interference method can conveniently detect the corresponding order without borrowing redundant devices.

ACKNOWLEDGMENTS

This work is supported by the National Natural Science Foundation of China (Grants No. 62005317, No. 12105366, No. 11704411, No. 11975022, No. 12072366, and No. 62005207); National Key Research and Development Program of China (Grant No. 2020YFA0713504); National Magnetic Confinement Fusion Program of China (Grant No. 2018YFE0310400); Natural Science Foundation of Hunan Province (Grants No. 2019JJ40341 and No. 2021JJ40695); Natural Science Foundation of Anhui Province (Grant No. 1908085MA26); Natural Science Foundation of Shanxi Province (Grant No. 2019JQ-648). The authors acknowledge assistance of Peng Xiong, Zhaohua Dong, and Jun-yi Du from Xidian University.

[1] Q. Zhan, Cylindrical vector beams: From mathematical concepts to applications, Adv. Opt. Photonics **1**, 1 (2009).
[2] Miles J. Padgett, Orbital angular momentum 25 years on [Invited], Opt. Express **25**, 11265 (2017).
[3] U. Levy, Y. Silberberg, and N. Davidson, Mathematics of vectorial Gaussian beams, Adv. Opt. Photonics **11**, 828 (2019).
[4] M. Dong, C. Zhao, Y. Cai, and Y. Yang, Partially coherent vortex beams: Fundamentals and applications, Sci. China Phys. Mech. **64**, 224201 (2021).
[5] Qiwen Zhan, Trapping metallic Rayleigh particles with radial polarization, Opt. Express **12**, 3377 (2004).
[6] E. Otte and C. Denz, Optical trapping gets structure: Structured light for advanced optical manipulation, Appl. Phys. Rev. **7**, 041308 (2020).
[7] Yuanjie Yang, Yuxuan Ren, Mingzhou Chen, Yoshihiko Arita, and Carmelo Rosales-Guzmán, Optical trapping with structured light: A review, Adv. Photonics **3**, 034001 (2021).
[8] Yuqiu Zhang, Tianyue Hou, Hongxiang Chang, Tao Yu, Qi Chang, Man Jiang, Pengfei Ma, Rongtao Su, and Pu Zhou, Tight focusing properties and focal field tailoring of cylindrical vector beams generated from a linearly polarized coherent beam array, Opt. Express **29**, 5259 (2021).
[9] H.-F. Xu, R. Zhang, Z.-Q. Sheng, and J. Qu, Focus shaping of partially coherent radially polarized vortex beam with tunable topological charge, Opt. Express **27**, 23959 (2019).
[10] M. Meier, V. Romano, and T. Feurer, Material processing with pulsed radially and azimuthally polarized laser radiation, Appl. Phys. A **86**, 329 (2007).
[11] Rokas Drevinskas, Jingyu Zhang, Martynas Beresna, Mindaugas Gecevičius, Andrey G. Kazanskii, Yuri P. Svirko, and Peter G. Kazansky, Laser material processing with tightly focused cylindrical vector beams, Appl. Phys. Lett. **108**, 221107 (2016).
[12] S. Segawa, Y. Kozawa, and S. Sato, Resolution enhancement of confocal microscopy by subtraction method with vector beams, Opt. Lett. **39**, 3118 (2014).
[13] K. Yuichi and S. Sato, Numerical analysis of resolution enhancement in laser scanning microscopy using a radially polarized beam, Opt. Express **23**, 2076 (2015).
[14] G. Milione, M. P. J. Lavery, H. Huang, Y. Ren, G. Xie, T. A. Nguyen, E. Karimi, L. Marrucci, D. A. Nolan, R. R. Alfano, and A. E. Willner, 4×20 Gbit/s mode division multiplexing over free space using vector modes and a q-plate mode (de)multiplexer, Opt. Lett. **40**, 1980 (2015).
[15] Chaofeng Wang, Bo Yang, Menglong Cheng, Sihang Cheng, Junmin Liu, Jiangnan Xiao, Huapeng Ye, Ying

Li, Dianyuan Fan, and Shuqing Chen, Cylindrical vector beam multiplexing for radio-over-fiber communication with dielectric metasurfaces, Opt. Express **28**, 38666 (2020).

[16] N. Bozinovic, Y. Yue, Y. Ren, T. P. Kristensen, H. Huang, A. E. Willner, and S. Ramachandran, Terabit-scale orbital angular momentum mode division multiplexing in fibers, Science **340**, 1545 (2013).

[17] Jian Wang, Advances in communications using optical vortices, Photonics Res. **4**, B14 (2016).

[18] A. E. Willner, H. Huang, Y. Yan, Y. Ren, N. Ahmed, G. Xie, C. Bao, L. Li, Y. Cao, Z. Zhao, J. Wang, M. P. J. Lavery, M. Tur, S. Ramachandran, A. F. Molisch, N. Ashrafi, and S. Ashrafi, Optical communications using orbital angular momentum beams, Adv. Opt. Photonics **7**, 66 (2015).

[19] X.-L. Wang, X.-D. Cai, Z.-E. Su, M.-C. Chen, D. Wu, L. Li, N.-L. Liu, C.-Y. Lu, and J.-W. Pan, Quantum teleportation of multiple degrees of freedom of a single photon, Nature **518**, 516 (2015).

[20] A. Sit, F. Bouchard, R. Fickler, J. Gagnon-Bischoff, H. Larocque, K. Heshami, D. Elser, C. Peuntinger, K. Günthner, B. Heim, C. Marquardt, G. Leuchs, R. W. Boyd, and E. Karimi, High-dimensional intracity quantum cryptography with structured photons, Optica **4**, 1006 (2017).

[21] J. Leach, B. Jack, J. Romero, A. K. Jha, A. Yao, S. Franke-Arnold, D. G. Ireland, R. W. Boyd, S. M. Barnett, and M. J. Padgett, Quantum correlations in optical angle-orbital angular momentum variables, Science **329**, 662 (2010).

[22] G. Vallone, V. D'Ambrosio, A. Sponselli, S. Slussarenko, L. Marrucci, F. Sciarrino, and P. Villoresi, Free-Space Quantum Key Distribution by Rotation-Invariant Twisted Photons, Phys. Rev. Lett. **113**, 060503 (2014).

[23] S. N. Khonina, A. V. Ustinov, and S. A. Degtyarev, Inverse energy flux of focused radially polarized optical beams, Phys. Rev. A **98**, 043823 (2018).

[24] S. Degtyarev, D. Savelyev, S. Khonina, and N. Kazanskiy, Metasurfaces with continuous ridges for inverse energy flux generation, Opt. Express **27**, 15129 (2019).

[25] Lipeng Feng, Yan Li, Sihan Wu, Xun Guan, Chen Yang, Weijun Tong, Wei Li, Jifang Qiu, Xiaobin Hong, Yong Zuo, Hongxiang Guo, Erhu Chen, and Jian Wu, All-fiber generation of arbitrary cylindrical vector beams on the first-order Poincaré sphere, Photonics Res. **8**, 1268 (2020).

[26] Zhipeng Dong, Yimin Zhang, Hongxun Li, Runxia Tao, Chun Gu, Peijun Yao, Qiwen Zhan, and Lixin Xu, All-fiber cylindrical vector beams laser based on the principle of mode superposition, Opt. Laser Technol. **139**, 106965 (2021).

[27] Yoel Sebbag and Uriel Levy, Arbitrarily directed emission of integrated cylindrical vector vortex beams by geometric phase engineering, Opt. Lett. **45**, 6779 (2020).

[28] Kenan Cicek, Ziyang Hu, Jiangbo Zhu, Laura Meriggi, Shimao Li, Zhichao Nong, Shengqian Gao, Ning Zhang, Xuyang Wang, Xinlun Cai, Marc Sorel, and Siyuan Yu, Integrated optical vortex beam receivers, Opt. Express **24**, 28529 (2016).

[29] Fufei Pang, Lina Xiang, Huanhuan Liu, Liang Zhang, Jianxiang Wen, Xianglong Zeng, and Tingyun Wang, Review on fiber-optic vortices and their sensing applications, J. Lightwave Technol. **39**, 3740 (2021).

[30] D. M. Fatkhiev, M. A. Butt, E. P. Grakhova, R. V. Kutluyarov, I. V. Stepanov, N. L. Kazanskiy, S. N. Khonina, V. S. Lyubopytov, and A. K. Sultanov, Recent advances in generation and detection of orbital angular momentum optical beams: A review, Sensors **21**, 4988 (2021).

[31] K. J. Moh, X. C. Yuan, J. Bu, D. K. Y. Low, and R. E. Burge, Direct noninterference cylindrical vector beam generation applied in the femtosecond regime, Appl. Phys. Lett. **89**, 251114 (2006).

[32] Junli Qi, Hui Zhang, Baoguo Pan, Haifei Deng, Jinhong Yang, Bo Shi, Hui Wang, Ang Du, Weihua Wang, and Xiujian Li, A succinct method to generate multi-type HCV beams with a spatial spiral varying retardation-plate, Europhys. Lett. **121**, 54004 (2018).

[33] S. N. Khonina, A. V. Ustinov, S. A. Fomchenkov, and A. P. Porfirev, Formation of hybrid higher-order cylindrical vector beams using binary multi-sector phase plates, Sci. Rep. **8**, 14320 (2018).

[34] W. Lee, X. Yuan, and W. Cheong, Optical vortex beam shaping by use of highly efficient irregular spiral phase plates for optical micromanipulation, Opt. Lett. **29**, 1796 (2004).

[35] W. Wu, Z. Sheng, and H. Wu, Design and application of flat spiral phase plate, Acta Phys. Sin. **68**, 054102 (2019).

[36] C. Loussert and E. Brasselet, Efficient scalar and vectorial singular beam shaping using homogeneous anisotropic media, Opt. Lett. **35**, 7 (2010).

[37] S. N. Khonina, A. P. Porfirev, and N. L. Kazanskiy, Variable transformation of singular cylindrical vector beams using anisotropic crystals, Sci. Rep. **10**, 5590 (2020).

[38] L. Marrucci, C. Manzo, and D. Paparo, Optical Spin-to-Orbital Angular Momentum Conversion in Inhomogeneous Anisotropic Media, Phys. Rev. Lett. **96**, 163905 (2006).

[39] Xiaohui Ling, Huiling Luo, Fuxin Guan, Xinxing Zhou, Hailu Luo, and Lei Zhou, Vortex generation in the spin-orbit interaction of a light beam propagating inside a uniaxial medium: Origin and efficiency, Opt. Express **28**, 27258 (2020).

[40] S. N. Khonina and S. V. Karpeev, Generating inhomogeneously polarized higher-order laser beams by use of diffractive optical elements, J. Opt. Soc. Am. A **28**, 2115 (2011).

[41] S. N. Khonina, S. V. Karpeev, and A. P. Porfirev, Sector sandwich structure: An easy-to-manufacture way towards complex vector beam generation, Opt. Express **28**, 27628 (2020).

[42] L. Stoyanov, S. Topuzoski, I. Stefanov, L. Janicijevic, and A. Dreischuh, Far field diffraction of an optical vortex beam by a fork-shaped grating, Opt. Commun. **350**, 301 (2015).

[43] K. J. Mitchell, S. Turtaev, M. J. Padgett, T. Cizmar, and D. B. Phillips, High- speed spatial control of the intensity, phase and polarisation of vector beams using a digital micro-mirror device, Opt. Express **24**, 29269 (2016).

[44] Xiang-Yu Zeng, Yu-Qin Zhang, Rui-Rui Zhang, Xiao-Rong Ren, Zi-Jun Zhan, Man-Na Gu, Rui Sun, Chun-Xiang Liu, and Chuan-Fu Cheng, Generation of vector beams of Bell-like states by manipulating vector vortex modes with plasmonic metasurfaces, Opt. Lett. **46**, 528 (2021).

[45] R. Dharmavarapu, K. Izumi, I. Katayama, S. H. Ng, J. Vongsvivut, M. J. Tobin, A. Kuchmizhak, Y. Nishijima,

S. Bhattacharya, and S. Juodkazis, Dielectric cross-shaped resonator based metasurface for vortex beam generation in mid-IR and THz wavelengths, Nanophotonics **8**, 1263 (2019).

[46] S. Chen, Y. Cai, G. Li, S. Zhang, and K. W. Cheah, Geometric metasurface fork gratings for vortex-beam generation and manipulation, Laser Photonics Rev. **10**, 322 (2016).

[47] B. Liu, Y. He, S.-W. Wong, and Y. Li, Multifunctional vortex beam generation by a dynamic reflective metasurface, Adv. Opt. Mater. **9**, 2001689 (2021).

[48] X. Zhang, L. Huang, R. Zhao, Q. Wei, X. Li, G. Geng, J. Li, X. Li, Y. Wang, and S. Zhang, Multiplexed generation of generalized vortex beams with on-demand intensity profiles based on metasurfaces, Laser Photonics Rev. **16**, 2100451 (2022).

[49] W. Shu, X. Ling, X. Fu, Y. Liu, Y. Ke, and H. Luo, Polarization evolution of vector beams generated by *q*-plates, Photonics Res. **5**, 64 (2017).

[50] A. Rubano, F. Cardano, B. Piccirillo, and L. Marrucci, *Q*-plate technology: A progress review [Invited], J. Opt. Soc. Am. B **36**, D70 (2019).

[51] V. G. Niziev, R. S. Chang, and A. V. Nesterov, Generation of inhomogeneously polarized laser beams by use of a Sagnac interferometer, Appl. Opt. **45**, 8393 (2006).

[52] P. Li, Y. Zhang, S. Liu, C. Ma, L. Han, H. Cheng, and J. Zhao, Generation of perfect vectorial vortex beams, Opt. Lett. **41**, 2205 (2016).

[53] X. Xu, Y. Zhou, Y. S. Yuan, J. Wang, H. F. Xu, and J. Qu, Generation of cylindrical and elliptical symmetrical vector beam on the Mach–Zehnder interferometer, AIP Adv. **8**, 125007 (2018).

[54] Chao Chen, Yu Zhang, Li Ma, Yuqin Zhang, Zhenhua Li, Ruirui Zhang, Xiangyu Zeng, Zijun Zhan, Changwei He, Xiaorong Ren, Chuanfu Cheng, and Chunxiang Liu, Flexible generation of higher-order Poincaré beams with high efficiency by manipulating the two eigenstates of polarized optical vortices, Opt. Express **28**, 10618 (2020).

[55] K. Huang, H. Liu, F. J. Garcia-Vidal, M. Hong, B. Luk'yanchuk, J. Teng, and C. W. Qiu, Ultrahigh-capacity non-periodic photon sieves operating in visible light, Nat. Commun. **6**, 7059 (2015).

[56] R. Liu, F. Li, M. J. Padgett, and D. B. Phillips, Generalized photon sieves: Fine control of complex fields with simple pinhole arrays, Optica **2**, 1028 (2015).

[57] Junli Qi, Wenchao Sun, Jiali Liao, Yongming Nie, Xiaofeng Wang, Jun Zhang, Xishun Liu, Hui Jia, Min Lu, Shaorong Chen, Ju Liu, Jiankun Yang, Jichun Tan, and Xiujian Li, Generation and analysis of both in-phase and out-phase radially polarized femtosecond-pulse beam, Opt. Eng. **52**, 024201 (2013).

[58] P. Panthong, S. Srisuphaphon, A. Pattanaporkratana, S. Chiangga, and S. Deachapunya, A study of optical vortices with the Talbot effect, J. Opt. **18**, 035602 (2016).

[59] Sheng Liu, Shuxia Qi, Yi Zhang, Peng Li, Dongjing Wu, Lei Han, and Jianlin Zhao, Highly efficient generation of arbitrary vector beams with tunable polarization, phase, and amplitude, Photonics Res. **6**, 228 (2018).

[60] S. N. Khonina, A. V. Ustinov, and A. P. Porfirev, Vector Lissajous laser beams, Opt. Lett. **45**, 4112 (2020).

[61] S. Choomdaeng, N. Chattham, and A. Pattanapokratana, Characteristics of fork fringes formed by two obliquely-incident vortex beams with different topological charge number, J. Phys. Conf. Ser. **1144**, 012158 (2018).

[62] P. Kumar and N. K. Nishchal, Modified Mach-Zehnder interferometer for determining the high-order topological charge of Laguerre-Gaussian vortex beams, J. Opt. Soc. Am. A **36**, 1447 (2019).

[63] Jingbo Ma, Peng Li, Ziheng Zhou, and Yuzong Gu, Characteristics of fork-shaped fringes formed by off-axis interference of two vortex beams, J. Opt. Soc. Am. A **38**, 115 (2021).

[64] S. Slussarenko, V. D' Ambrosio, B. Piccirillo, L. Marrucci, and E. Santamato, The polarizing Sagnac interferometer: a tool for light orbital angular momentum sorting and spin-orbit photon processing, Opt. Express **18**, 27205 (2010).

[65] S. W. Cui, B. Xu, S. Y. Luo, H. Y. Xu, Z. P. Cai, Z. Q. Luo, J. X. Pu, and S. Chávez-Cerda, Determining topological charge based on an improved Fizeau interferometer, Opt. Express **27**, 12774 (2019).

[66] Q. Zhao, M. Dong, Y. H. Bai, and Y. J. Yang, Measuring high orbital angular momentum of vortex beams with an improved multipoint interferometer, Photonics Res. **8**, 745 (2020).

[67] O. Emile and J. Emile, Young's double-slit interference pattern from a twisted beam, Optica **2**, 1028 (2015).

[68] J. Qi, W. Wang, X. Li, X. Wang, W. Sun, J. Liao, and Y. Nie, Double-slit interference of radially polarized vortex beams, Opt. Eng. **53**, 44107 (2014).

[69] T. Chen, X. Lu, J. Zeng, Z. Wang, H. Zhang, C. Zhao, B. J. Hoenders, and Y. Cai, Young's double-slit experiment with a partially coherent vortex beam, Opt. Express **28**, 38106 (2020).

[70] P. Panthong, S. Srisuphaphon, S. Chiangga, and S. Deachapunya, High-contrast optical vortex detection using the Talbot effect, Appl. Opt. **57**, 1657 (2018).

[71] S. Srisuphaphon, S. Buathong, and S. Deachapunya, Realization of an optical vortex from light-emitting diode source by a vortex half-wave retarder and using Talbot effect based detection, Optics Laser Technol. **148**, 107746 (2022).

[72] B. Lan, C. Liu, D. M. Rui, M. Chen, F. Shen, and H. Xian, The topological charge measurement of the vortex beam based on dislocation self-reference interferometry, Phys. Scripta **94**, 055502 (2019).

[73] P. Kumar and N. K. Nishchal, Self-referenced interference of laterally displaced vortex beams for topological charge determination, Opt. Commun. **459**, 125000 (2020).

[74] L. E. E. De Araujo and M. E. Anderson, Measuring vortex charge with a triangular aperture, Opt. Lett. **36**, 787 (2011).

[75] Y. Liu, H. Tao, J. Pu, and B. Lu, Detecting the topological charge of vortex beams using an annular triangle aperture, Opt. Laser Technol. **43**, 1233 (2011).

[76] C. S. Guo, L. L. Lu, and H. T. Wang, Characterizing topological charge of optical vortices by using an annular aperture, Opt. Lett. **34**, 3686 (2009).

[77] H. Tao, Y. Liu, Z. Chen, and J. Pu, Measuring the topological charge of vortex beams by using an annular ellipse aperture, Appl. Phys. B **106**, 927 (2012).

[78] Y. X. Liu, S. H. Sun, J. X. Pu, and B. D. Lv, Propagation of an optical vortex beam through a diamond-shaped aperture, Opt. Laser Technol. **45**, 473 (2013).

[79] J. P. C. Narag and N. Hermosa, Probing Higher Orbital Angular Momentum of Laguerre-Gaussian Beams via Diffraction Through a Translated Single Slit, Phys. Rev. Appl. **11**, 054025 (2019).

[80] C. S. Guo, S. J. Yue, and G. X. Wei, Measuring the orbital angular momentum of optical vortices using a multipinhole plate, Appl. Phys. Lett. **94**, 231104 (2009).

[81] K. Dai, C. Gao, L. Zhong, Q. Na, and Q. Wang, Measuring OAM states of light beams with gradually-changing-period gratings, Opt. Lett. **40**, 562 (2015).

[82] Z. Shuang and J. Wang, Measuring orbital angular momentum (OAM) states of vortex beams with annular gratings, Sci. Rep. **7**, 40781 (2017).

[83] M. L. Chen, L. Jiang, and W. Sha, Orbital angular momentum generation and detection by geometric-phase based metasurfaces, Appl. Sci. **8**, 362 (2018).

[84] Y. Guo, S. Zhang, M. Pu, Q. He, J. Jin, M. Xu, Y. Zhang, P. Gao, and X. Luo, Spin-decoupled metasurface for simultaneous detection of spin and orbital angular momenta via momentum transformation, Light-Sci. Appl. **10**, 63 (2021).

[85] G. C. G. Berkhout, M. P. J. Lavery, J. Courtial, M. W. Beijersbergen, and M. J. Padgett, Efficient Sorting of Orbital Angular Momentum States of Light, Phys. Rev. Lett. **105**, 153601 (2010).

[86] G. C. G. Berkhout, M. P. J. Lavery, M. J. Padgett, and M. W. Beijersbergen, Measuring orbital angular momentum superpositions of light by mode transformation, Opt. Lett. **36**, 1863 (2011).

[87] M. I. Dedo, Z. Wang, K. Guo, and Z. Guo, OAM mode recognition based on joint scheme of combining the Gerchberg-Saxton (GS) algorithm and convolutional neural network (CNN), Opt. Commun. **456**, 124696 (2020).

[88] Z. Liu, S. Yan, H. Liu, and X. Chen, Superhigh-Resolution Recognition of Optical Vortex Modes Assisted by a Deep-Learning Method, Phys. Rev. Lett. **123**, 183902 (2019).

[89] Yihua Bai, Haoran Lv, Xin Fu, and Yuanjie Yang, Vortex beam: Generation and detection of orbital angular momentum [Invited], Chin. Opt. Lett. **20**, 012601 (2022).

[90] S. Deachapunya, S. Srisuphaphon, and S. Buathong, Production of orbital angular momentum states of optical vortex beams using a vortex half-wave retarder with double-pass configuration, Sci. Rep. **12**, 6061 (2022).

[91] J. Qi, W. Wang, B. Shi, H. Zhang, Y. Shen, H. Deng, W. Pu, X. Liu, H. Shan, X. Ma, L. Zhang, W. Lu, M. Fu, and X. Li, Concise and efficient direct-view generation of arbitrary cylindrical vector beams by a vortex half-wave plate, Photonics Res. **9**, 803 (2021).

[92] J. Qi, W. Yi, M. Fu, M. Zhu, J. Liu, G. Huang, J. Pan, S. Zhu, X. Chen, W. Tabg, H. Zhang, B. Shi, H. Deng, W. Wang, and X. Li, Practical generation of arbitrary high-order cylindrical vector beams by cascading vortex half-wave plates, Opt. Express **29**, 25365 (2021).